Article

Unprecedented recent summer warming and cross-sphere hydrological coupling in Asian Water Towers

Check for updates

Youping Chen[1,2,3,4], Feng Chen[1,2,3] ✉, Mao Hu[1,2,3], Xiaoen Zhao[1,2,3], Honghua Cao[1,2,3], Shijie Wang[1,2],
Jan Esper[5,6], Ulf Büntgen[6,7,8], Max C. A. Torbenson[5], Tiyuan Hou[1,2], Hongfan Xu[1,2,3] & Yufeng Lin[1,2]

The Asian Water Towers play a crucial role by storing and releasing vast amounts of freshwater, thereby sustaining the base flow of major Asian rivers and water security for billions of people at sub-continent to hemispheric scales. Instrumental records, though spatially and temporally limited, indicate rapid warming in High Asia. However, the sensitivity and long-term resilience of these Water Towers remain uncertain. Here, we use an 814-year-long tree-ring record (including tree-ring width and maximum latewood density) from *Picea likiangensis* on the eastern Tibetan Plateau to develop a summer (June-September) temperature reconstruction. Our reconstruction reveals that the series has warmed by 1.5 °C during the modern observational period (1970–2023), which is 0.5 ± 0.4 °C above the pre-industrial baseline (1210–1850 or 1850-1900), making the summer of 2024 the warmest in the past eight centuries. This unprecedented warming amplifies winter runoff in the Brahmaputra, Indus, and Salween headwaters through a cascade of atmosphere-cryosphere feedbacks: enhanced meltwater and spring soil-moisture persistence promote earlier and lusher vegetation growth, which reduces summer albedo and further accelerates regional warming. Detection and attribution analyses identify volcanic and solar forcing as the main drivers of natural, pre-industrial variability before 1850 CE, whereas anthropogenic forcing is detected with high confidence (exceeding the 99% confidence level) after 2020 CE.

The major Asian rivers, such as the Mekong, Brahmaputra, Indus, Salween, Yellow, Ganges, and Yangtze originate from the Tibetan Plateau and its adjacent mountain systems. Known as the Asian Water Towers, these regions provide essential water resources for more than two billion people in the downstream watersheds[1–5]. It is therefore important to understand how streamflow regimes respond to climate change to adapt agricultural systems and socioeconomic structures for the wellbeing of an ever-growing human population. Despite inconsistencies in the magnitude of water resource availability, most studies predict the runoff of the main rivers to increase under global warming[5–9]. The principal mechanisms are increased glacier melting and an acceleration of the water cycle due to warming-induced convective summer precipitation[1,8,10]. Although several studies have noted the importance of temperature changes for the water cycle in High Asia and

elsewhere[1,9], the direct and indirect responses of regional streamflow regimes to rising temperatures are not fully understood.

To address the limited length and spatial coverage of instrumental records and to evaluate temperature–runoff sensitivity on centennial timescales, high-resolution paleoclimate reconstructions are needed; tree-ring provides annually resolved proxies well suited to this task. While previous research has effectively reconstructed millennium-scale streamflow variability and established its ecological and societal impacts downstream[11], the upstream climatic drivers—particularly the thermal mechanisms governing this variability—remain relatively understudied. Although tree-ring width (TRW) measurements have been used to constrain the range of temperature changes for the Asian Water Towers during the past millennium[12–17], more precise maximum latewood density (MXD)

[1]Yunnan Key Laboratory of International Rivers and Transboundary Eco-Security/Ministry of Education Key Laboratory for Transboundary Eco-Security of Southwest China, Institute of International Rivers and Eco-Security, Yunnan University, Kunming, China. [2]State Key Laboratory of Vegetation Structure, Functions and Construction (VegLab), Yunnan University, Kunming, China. [3]Southwest United Graduate School, Kunming, China. [4]School of Ecology and Environmental Science, Yunnan University, Kunming, China. [5]Department of Geography, Johannes Gutenberg University, Mainz, Germany. [6]Global Change Research Institute (CzechGlobe), Czech Academy of Sciences, Brno, Czechia. [7]Department of Geography, University of Cambridge, Cambridge, UK. [8]Department of Geography, Faculty of Science, Masaryk University, Brno, Czechia. ✉e-mail: feng653@163.com

Fig. 1 | Temperature reconstruction and source material. a Map illustrating the study area with tree-ring sampling sites and observational stations in the Indus, Brahmaputra, and Salween basins. Background colors indicate first-order difference correlations ($p < 0.05$, two-tailed) between the density chronologies with gridded June–September temperatures from 1970 to 2023. Map created using ArcGIS v10.8. **b** Balfour spruce sampled at the Jionglacuo outlet (photo by Tiyuan Hou, taken on June 15, 2024). **c** Jionglacuo and the ice tongue in contact with it (photo by Youping Chen, taken on June 15, 2024). **d** June–September temperature reconstruction back to 1210 CE at annual resolution, and after smoothing using a 21-year low-pass filter (black curve). The gray band surrounding the reconstruction is the ±2 standard deviation (±2 SD).
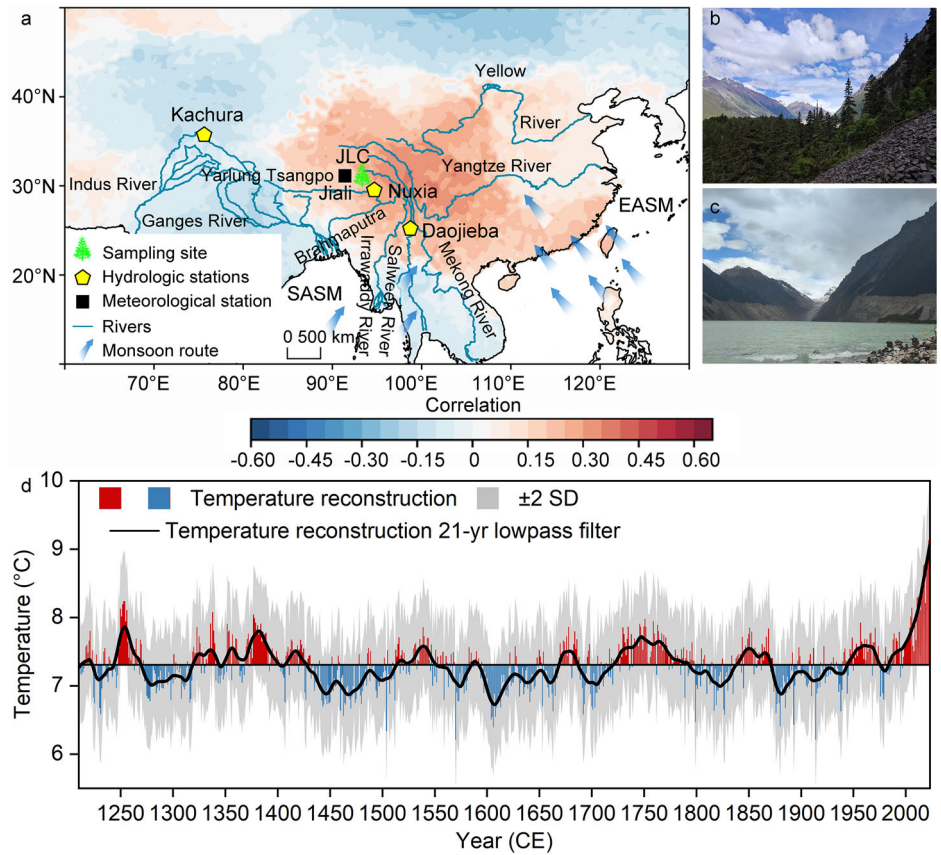
measurements are still limited for the Tibetan Plateau. Here, we combine TRW and MXD chronologies to reconstruct summer temperatures back to 1210 CE. We then compare the newly developed temperature history with streamflow variability to deepen understanding of the sensitivity of the Asian Water Towers to anthropogenic climate change.

Results and discussion

Tree-ring-reconstructed temperature

We present an annually resolved and absolutely dated 814-year-long reconstruction of mean June–September (JJAS) temperatures based on 31 living Balfour spruce (*Picea likiangensis*) trees (Supplementary Figs. 1, 2 and Supplementary Table 1) growing near a glacial lake of the upper Salween River in the border zone of the eastern Tibetan Canyon and the northern Tibetan Plateau (Fig. 1 and Supplementary Fig. 3). Growing on glacier moraines above 3000 m asl, both TRW and MXD are strongly correlated with summer temperatures (Supplementary Fig. 4). The reconstruction model was calibrated against instrumental data for the period 1970–2023, a period that provides the best available overlap between high-quality tree-ring and meteorological records in this remote region (Supplementary Fig. 5b, d, f). The statistical skill of the calibration (see Methods) and the strong coherence of our record with independent temperature reconstructions support the stability of the climate-proxy relationship (Supplementary Fig. 6 and Supplementary Table 2).

Our new reconstruction reveals warm summers during the late medieval period, particularly in the 13th and 14th centuries, interrupted by a rapid cooling in 1258 CE following the 1257CE Samalas eruption. It displays considerable interdecadal variability during the generally cooler period between the 15th and 17th centuries, associated with Little Ice Age Type Events[18,19]. After a colder 17th century, summers remained relatively warm until the late 18th century, before cooler conditions prevailed from the 1790 s to the 1830s. In line with the instrumental measurements from the nearby Jiali station, temperatures increased persistently since the 1870s.

Over the most recent observational window (1970–2023), the reconstructed series warmed by 1.5 °C, yielding a post-1970 mean of 7.8 °C. This represents a 0.5 ± 0.4 °C increase relative to the pre-industrial baseline of 7.3 °C (defined as either 1210–1850 or 1850–1900) (Fig. 2a, f). Notably, the 2024 mean reached 9.6 °C, making the summer of 2024 the warmest in the entire 814-year record.

Contextualizing recent warming

Comparison of our spruce TRW and MXD composite (Fig. 2a) with two independent regional reconstructions—(i) a multi-species TRW record from the eastern Tibetan Plateau[12] (Fig. 2b) and (ii) an MXD record from the southeastern Tibetan Plateau[20] (Fig. 2c)—demonstrates highly significant coherence across the past eight centuries ($r = 0.24$, $n = 796$; $r = 0.23$, $n = 763$; $p < 0.001$ for both). However, as these correlation coefficients account for a limited portion of the total variance, we further assessed the temporal coherence using 21-year low-pass filtered series. The correlations on this multi-decadal timescale are stronger ($r = 0.24$ and $r = 0.35$), indicating markedly improved agreement for lower-frequency variability. The fact that our record integrates both growth-ring width and wood density, whereas the comparison series rely on a single parameter, yet all three capture the same multidecadal swings and the dramatic post-1970 warming (box plots in Fig. 2f–h), collectively attests to the credibility of the new reconstruction. The observed differences in the raw series, which are expected given the distinct proxies, sites, and methodologies employed, are also evident in all frequency domains. These differences include estimates during the Dalton solar minimum[21], for which our new reconstruction suggests relatively warm conditions, and muted decadal variability prior to 1600 CE in the latter. Both the TRW and MXD of spruce in Jionglacuo accurately record the recent warming trend, without any sign of the so-called 'Divergence Phenomenon'[22]. While generally consistent with the 'Medieval Climate Anomaly' (MCA), 'Little Ice Age' (LIA), and the 'Modern Anthropogenic Warming Period' (MAWP) observed in Northern Hemisphere temperature

Fig. 2 | Climatic context of the new reconstruction.
a Reconstructed June–September temperatures (thin gray curve) and 21-year low-pass filter (thick black curve). **b** Reconstructed June–August temperatures (thin gray curve) 21-year low-pass filter (thick black curve) from the eastern Tibetan Plateau[12]. **c** Reconstructed August-September temperatures (thin gray curve) 21-year low-pass filter (thick black curve) from the southeastern Tibetan Plateau[20]. **d** Reconstructed total solar irradiance (TSI)[21] including the main solar minima over the past 800 years. **e** Eruptions exceeding a volcanic explosivity index (VEI) ≥ 5 since 1210 CE. **f–i** Box plots corresponding to **a–d** summarizing data for the pre-industrial period (PI 1: 1210–1850 and PI 2: 1850–1900), and the Modern period (Modern: 1970–2023). **j** Superposed Epoch Analysis of reconstructed June–September temperatures (from **a**) relative to major eruptions shown in (**e**).
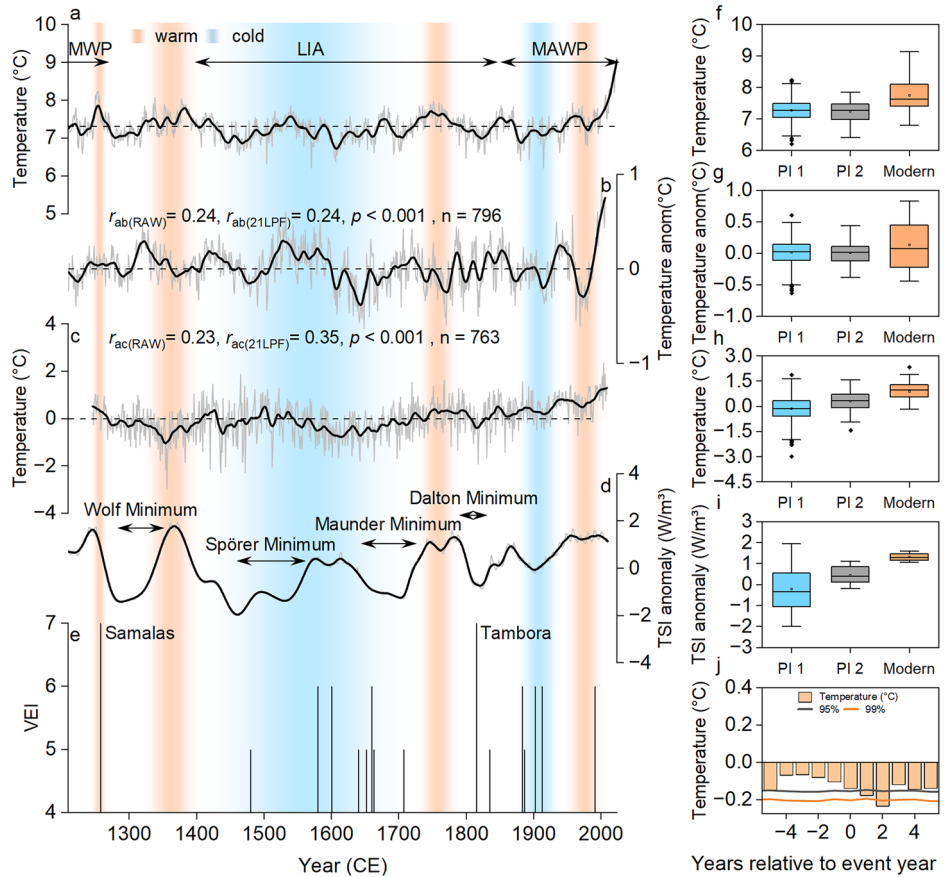
reconstructions over the past millennium[23], the temperature variations of the Asian Water Towers exhibit distinct characteristics. We acknowledge that the timing and expression of these periods may vary regionally[24,25]. For the southeastern Tibetan Plateau, we define the MCA as the period from 850 to 1270 CE and the LIA from 1400 to 1850 CE, based on previous studies[26] and our temperature reconstruction (Fig. 2). Although the MCA is less pronounced in our reconstruction and there is no gradual cooling trend from the MCA to the LIA, summer temperatures remained relatively warm throughout the periods of the 1240 s to 1260 s and 1320 s to 1420 s, and the cooling effect of the Samalas volcanic eruption in 1257 and the Wolf minimum was especially strong, almost interrupting the warmer conditions of the late MCA. The TRW/MXD-based estimates suggest cooler conditions from the 1420 s to the 1720 s, indicating the onset of the LIA in the early 15th century. This represents a significant shift, which is crucial for discussions on the potential drivers of Northern Hemisphere cooling[27] and the understanding of hydro-societal interactions. The cold periods of the 1790s–1830s and 1870s–1940s are likely also caused by the prominent interdecadal solar minima and superimposed clusters of volcanic eruptions (Fig. 2d, e, i, j, Supplementary Fig. 7 and Supplementary Table 3).

To examine the internal variability and external forces driving temperature changes on the Tibetan Plateau, we used the CESM-LME model data to construct a regression model with the external forcing variables of volcanic forcing (VOL), spectral solar irradiance (SSI), orbital parameters (ORB), land use/land cover (LULC), greenhouse gases (GHG), and ozone/aerosol (AERO, considered after 1850), together with the internal variability of the Interdecadal Pacific Oscillation (IPO), Indian Ocean Dipole (IOD), Atlantic Multidecadal Variability (AMV), and Arctic Oscillation (AO). The results are shown in Fig. 3a. Throughout the last millennium, external forcing dominates, with volcanic forcing being the main driver of temperature change, explaining 34.2% of temperature change. During the MCA and the LIA, volcanic forcing is similarly the main factor influencing

temperature change, explaining 36% and 40% of the variance in temperature, respectively. However, GHG and AMV are the principal factors influencing temperature change during the MAWP, explaining 37% and 33% of the variance in temperature, respectively. Since the recent temperature trend is included in the calculation of AMV, this high degree of explanation can be attributed to the synchronous change of temperature in Northern Hemisphere resulting in the anthropogenic GHG strongly influencing temperature change on the Tibetan Plateau during the MAWP.

To further evaluate anthropogenic influences on the temperature of the Tibetan Plateau, we combined the historical simulation of CMIP6 and the SSP585 simulation to produce a continuous series for the interval of 1850–2100 (Supplementary Table 4). We extracted the first principal component as the climatic fingerprint of GHG and calculated the time function of the spatial covariance between the gridded CRU temperature field and our reconstructed data and the fingerprint (see Methods, Supplementary Fig. 8). Finally, we obtained the measured data shown in Fig. 3b which detected a strong anthropogenic signal in the recent period, at the 66% confidence level near 2010, and at the 99% confidence level after 2020. This signal indicates that anthropogenic forcing plays an increasingly important role in climate change on the Tibetan Plateau. Recent studies have pointed out that the temperature changes in recent years are the most substantial in the past few centuries[17,28]. Hence, effective measures are required to mitigate extreme climatic events caused by human activities.

Coupling with winter streamflow
Of particular note is the significant seasonal lagged relationship between our new temperature reconstruction and observed streamflow from the Indus, Brahmaputra, and Salween Rivers over the period 1970–2010 (Supplementary Fig. 9). Specifically, we compare reconstructed June–September temperature anomalies with cold-season discharge (December–March) and early-winter discharge (January–February). Positive correlations peak in the

Fig. 3 | Climate forcing. a Partitioned variance (%, red shading) and 95% confidence intervals (gray shading) in CESM-LME-simulated temperature anomalies attributed to external forcings (volcanic activity (VOL), spectral solar irradiance (SSI), orbital parameters (ORB), land use/land cover (LULC), ozone/aerosol (AERO), greenhouse gases (GHG)) and internal variability (Interdecadal Pacific Oscillation (IPO), Indian Ocean Dipole (IOD), Atlantic Multidecadal Variability (AMV), Arctic Oscillation (AO)) during the Last Millennium (LM), Medieval Climate Anomaly (MCA), Little Ice Age (LIA), and Modern Anthropogenic Warming Period (MAWP). **b** Temporal evolution of the signal-to-noise ratio (SNR) from CRU observations and our reconstruction, with confidence thresholds (66%, 90%, 99%) indicating the dominance of anthropogenic forcing (GHG) over natural variability since 1850.
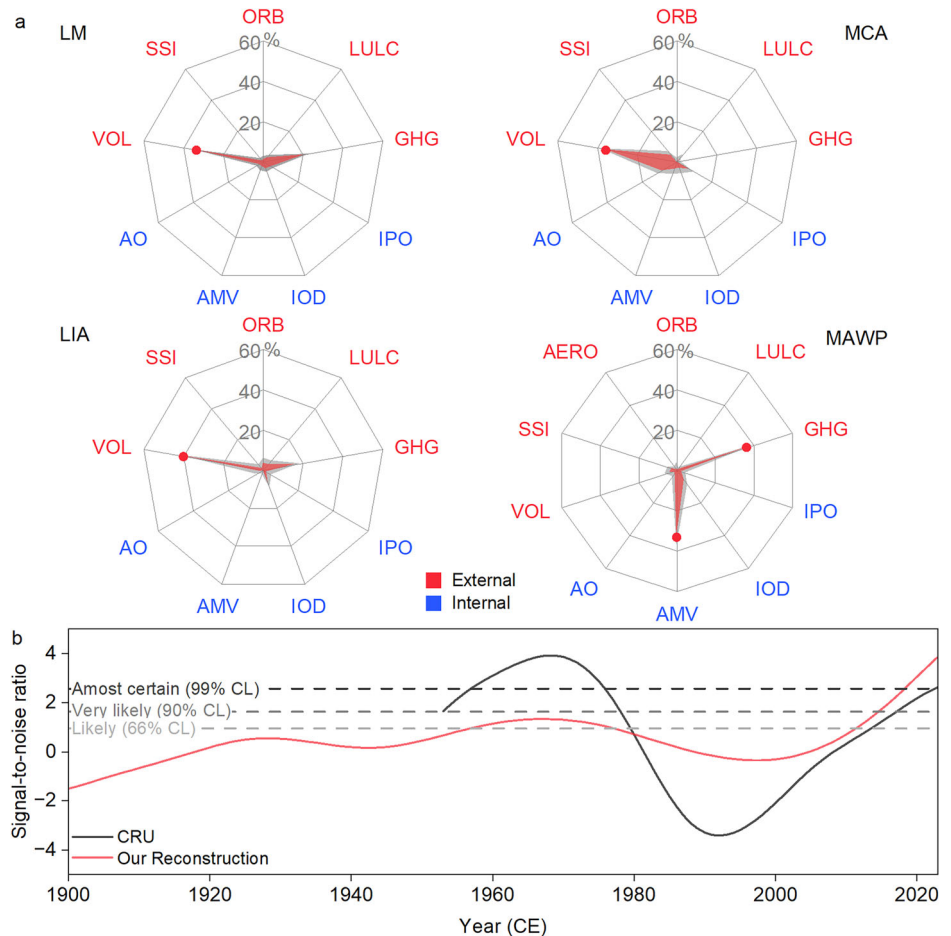
preceding winter (December–March; $r = 0.614$, $p < 0.01$) and remain significant, though weaker, into the current winter (January–February; $r = 0.336$, $p < 0.05$). These months coincide with the post-monsoon low-flow season, implying that years with elevated cold-season discharge are consistently followed by anomalously warm summers across the southeastern Tibetan Plateau. To further elucidate the dominant melt processes contributing to winter runoff, we note that in the upstream regions of major Tibetan rivers such as the Salween and Mekong, rainfall runoff constitutes the primary component of total annual flow, while snowmelt and glacial melt contribute smaller but hydrologically significant portions[29]. Although glacial melt runoff has increased significantly under warming, its contribution remains secondary to rainfall in controlling interannual streamflow trends. However, glacial melt plays a critical compensatory role during dry years, enhancing baseflow when precipitation is scarce. Snowmelt, while seasonally important, shows divergent trends across basins and does not consistently dominate the winter runoff response. Instead, the observed lagged correlation likely reflects integrated cryospheric and soil moisture dynamics—enhanced winter baseflow from meltwater and groundwater discharge promotes wetter conditions that precondition the land surface for stronger summer land-atmosphere coupling, rather than being directly driven by a single melt component.

The recent intensification of this coupling is evident. Figure 4a illustrates the probability distribution of reconstructed summer temperature anomalies for the pre-industrial period (1210–1850) compared to the modern period (2001–2023). The modern temperature anomalies are significantly warmer, falling outside the 99% confidence limit of the pre-industrial distribution. Each modern year is colored by its winter streamflow anomaly, revealing that years with the warmest summers consistently coincide with high winter streamflow, with several years experiencing runoff

surpluses exceeding 400 m³ s⁻¹ based on the correlation. In other words, streamflow has also surged to unprecedented levels in concert with the recent temperature escalation.

To test whether this linkage is a short-lived coincidence or a persistent feature of the regional hydro-climate, we compared the temperature reconstruction (1210–2020 CE) with an independent multi-basin reconstruction of previous September to current July streamflow for the Mekong, Salween and Brahmaputra[11] (Supplementary Fig. 10). Over the common 811-year interval the two raw series correlate at $r = 0.387$ ($p < 0.01$). Warm–wet and cold–dry years co-occur in 223 (27%) and 263 (32%) of the 811 years, respectively, including the Medieval Climate Anomaly (high temperature/high streamflow) and Little Ice Age (low temperature/low streamflow). Their 21-year low-pass curves track each other closely, underscoring a near-millennial-scale synchrony between thermal and hydrological variability. That co-evolution hints at stabilizing feedback embedded in the regional climate system.

To unravel the physical mechanisms behind this lagged relationship, we employed a structural equation model (SEM; Fig. 4b). The model parameters Chi-square, p, CFI, TLI and RMSEA were 6.33, 0.50, 1.00, 1.02 and 0.00, respectively, all indicating model validity. The analysis reveals two primary pathways through which high winter streamflow leads to warmer subsequent summers (Supplementary Table 5). First is the albedo pathway: High winter streamflow indicates ample moisture, which promotes a vigorous green-up of vegetation in spring[30]. The denser vegetation canopy has a lower albedo (i.e., it is darker), absorbing more solar radiation and leading to surface warming[31,32]. The second is the energy partitioning pathway: The increased soil moisture from winter reduces the energy used for evaporation (latent heat flux) in early summer. This diverts more incoming solar energy into heating the air (sensible heat flux), further warming the lower

Fig. 4 | Temperature–streamflow relationships.
a Probability distribution of recent temperature
anomalies (2001–2023) relative to the pre-industrial
baseline (1210–1850), with concurrent streamflow
deviations (1970–2010). Probability distribution
plot generated using Python v3.11.11 with SciPy
v1.15.3 and Matplotlib v3.10.0. **b** Structural equa-
tion model linking winter streamflow to subsequent
summer temperature. Variables include instru-
mental streamflow (Q_{P12-C3}), mean temperature
(Tm_{C6-C9}), normalized difference vegetation index
($NDVI_{C6-C9}$), soil moisture (SM_{C1-C9}), surface
albedo ($_{C6-C9}$), and latent heat flux (LHF_{C1-C9}). "P"
denotes the previous year and "C" the current year.
Red arrows indicate positive effects, blue arrows
indicate negative effects; ** and *** denote sig-
nificance at the 95% and 99% confidence levels,
respectively. The left-hand inset summarizes the
effects corresponding to the three main pathways—
A: Q-NDVI-Albedo-Tm; B: Q-SM-LHF-Tm; C: Q-
SM-NDVI-Albedo-Tm—and their total effect (TE).
c Conceptual model of synergistic changes in tem-
perature, streamflow, and tree-rings.
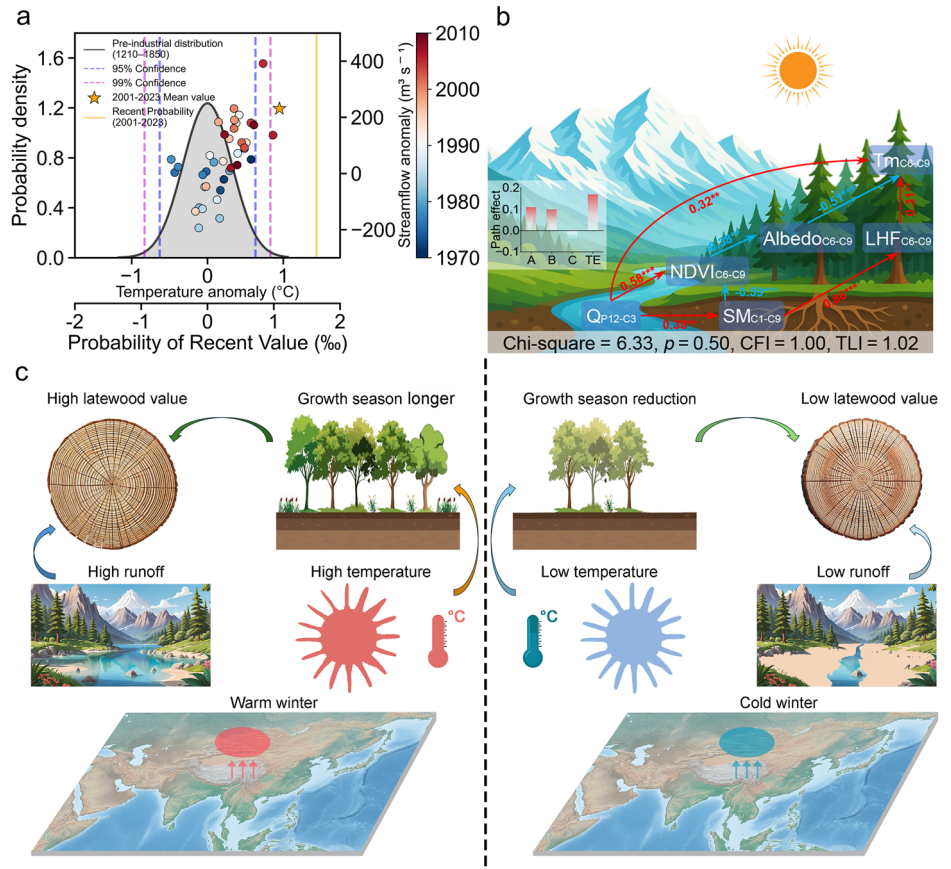
atmosphere[33]. This integration of processes, known as land-atmosphere
coupling, explains about one-third of the variance in summer temperature
—a performance comparable to other studies on the Tibetan Plateau[9,34].

The connection between our reconstructed temperature and runoff
series can further establish the possible baselines for simulating past and
future freshwater discharges over High Asia (Fig. 4). Our results show that
temperatures are currently higher than at any point in the past eight cen-
turies, indicating that global warming is now detectable even in one of the
most remote regions of the world. Similarly, the temperature-related
streamflow observed today may be unprecedented since Medieval times.
Due to warming leading to increased glacial meltwater streamflow[35], this
effect may be more pronounced in the inland water towers of the Tibetan
Plateau, which are less influenced by the Asian summer monsoon. It is
expected that water resource losses from the Asian Water Towers will
increase further under continued global warming.

Limitations
While this study offers a high-resolution, multi-century perspective on
summer warming and hydrological coupling in the southeastern Tibetan
Plateau, several limitations warrant consideration. Our reconstruction relies
on a single tree species from one site, which, despite strong regional
coherence, constrains spatial representativeness and cautions against
extrapolation across the heterogenous Asian Water Towers. Furthermore,
the inferred mechanisms linking winter streamflow to summer temperature
—though physically plausible and statistically supported—are derived from
correlative modeling and modern data; future process-based observations or
high-resolution model experiments are needed to confirm causality and
quantify contributions of albedo and energy partitioning pathways. Lastly,
while our attribution analysis robustly identifies anthropogenic influence
(exceeding 99% confidence post-2020), uncertainties in climate models—
particularly in representing topography–atmosphere interactions and

aerosol effects—affect precise forcing estimates. Nonetheless, the high
signal-to-noise ratio and consistency with physical principles support our
core conclusion of dominant anthropogenic warming in recent decades.

Methods
Tree-ring and climate data
In June 2024, we collected 79 core samples from 31 individuals of Balfour
spruce (*Picea likiangensis*) at Jionglacuo, Bianba County, Qamdo City,
Tibet Autonomous Region, China. The site is located on a northeast-facing
slope at 3951.8 m a.s.l., where a thin soil layer consisting mainly of dark-
brown earths, alpine meadow soil, and burozem overlies bedrock (Sup-
plementary Table 1). Standard dendrochronological methods[36,37] were
applied for sample preparation, including air-drying, mounting, sanding,
and cross-dating. Ring widths were measured with a precision of 0.001 mm
and verified using the COFECHA program[38]. 40 sample cores from 20 trees
without corrosion were subsequently prepared for densitometric analysis
following established protocols[39]. Cores were sectioned into 1.0 mm-thick
laths, X-rayed, and analyzed using the CooRecorder 9.4 software to obtain
measurements of tree-ring width and maximum latewood density, both of
which are reliable indicators for temperature reconstruction. To remove
age-related growth trends while retaining climate-related signals, the tree-
ring series were standardized into dimensionless indices using RCSsigFree
software[40]. TRW data were linearly detrended, while MXD data were fitted
with an age-dependent cubic spline set to a 50-year 50% frequency
response, and both underwent signal-free iterations to suppress common
biases. We employed biweight robust averaging to generate the final
chronologies, which reduces the influence of outliers and enhances the
reliability of the mean value estimation[37] (Supplementary Fig. 1a). The
reliability of the chronology was evaluated using the inter-series correlation
(Rbar) and the expressed population signal (EPS)[41] computed in 50-year
moving windows with 25-year overlap over the full length of the record.

EPS exceeds 0.85 consistently from 1210 CE onward, which we adopt as the reliable period. (Supplementary Fig. 1b). The chronologies of TRW and MXD were significantly correlated ($r = 0.545$, $p < 0.01$, 1210–2023), indicating that both reliably record temperature changes. To balance the high-frequency signal of TRW and the low-frequency signal of MXD, thereby improving the robustness of the reconstruction, a principal component analysis[42] was performed. According to the Kaiser criterion ($\lambda > 1$), we retained PC1 ($\lambda_1 = 1.545$; 77% of standardized variance), while PC2 ($\lambda_2 = 0.455$; 23%) was not used (Supplementary Fig. 2). Climate data, including monthly mean temperature, maximum temperature, minimum temperature, and precipitation, were obtained from Jiali Meteorological Station (Supplementary Fig. 3).

Temperature reconstructions and validation

Prior to defining the seasonal target, we quantified proxy–climate sensitivity at the monthly scale. Specifically, we computed Pearson correlations between each chronology (TRW, MXD, and their PC1) and monthly mean climate data from the Jiali station over 1970–2023. Response analysis indicates that TRW shows the strongest correlation with average temperatures from July to September ($r = 0.797$, $p < 0.01$), MXD correlates most strongly with average temperatures from June to September ($r = 0.826$, $p < 0.01$), while PC1 exhibits the strongest correlation with average temperatures from June to September ($r = 0.831$, $p < 0.01$) (Supplementary Fig. 4). After determining the seasonal mean temperature forcing for June to September of each year, we reconstructed the mean temperature of the study area using linear regression based on PC1. The calibration model is defined as:

$$T_{JJAS} = 0.362PC1 + 7.306 \qquad (1)$$

The model explains 69.0% of the variance in the observed JJAS temperatures over the full calibration period (1970–2023) (Supplementary Fig. 5). To ensure the stability of the relationship during 1970–2023 and avoid overfitting, we applied leave-one-out cross-validation[36] and split-sample climate calibration (Supplementary Table 2). The error reduction ratio (RE), product mean test (PMT), sign test (ST) for both calibration and validation sub-periods all indicate that the reconstructed model is stable. The Durbin-Watson statistic for the full-period model residuals was 1.714, indicating no significant levels of autocorrelation. Furthermore, to explicitly test the temporal stability of the proxy-climate relationship, we performed moving window calibration analysis with a 30-year window. The results show consistently strong and stable r values throughout the instrumental period (Supplementary Fig. 6), Cold and warm periods were identified based on a 21-year running mean that deviated from the 1210–2023 average for more than 10 consecutive years. It is important to note that this method may not fully capture the variability of extreme climate events, particularly in cases of abrupt temperature shifts. The spatial representativeness of the reconstruction was evaluated through correlation analysis with Climatic Research Unit gridded data (CRU Version 4.08) gridded mean temperature data[43]. To understand the climatic context, the reconstructed temperature series was compared with total solar irradiance[21], and its response to major volcanic eruptions and volcanic stratospheric sulfur injections[44] were further assessed using Superposed Epoch Analysis (SEA)[45]. Volcanic eruptions with a Volcanic Explosivity Index (VEI) ≥ 5 were identified from the Smithsonian Institution's volcanic activity catalog[46] (Supplementary Table 3). Volcanic stratospheric sulfur injections were selected from the eVolv2k database (Supplementary Fig. 7a)[47]. The year of peak volcanic aerosol mass was defined as Year 0, followed by Years 1 and 2, with anomalies calculated relative to the 5-year average preceding the eruptions[48]. As shown in Fig. 2j and Supplementary Fig. 7b, SEA indicates a significant cooling in annual temperatures during the first year following the volcanic eruption, with this phenomenon persisting into the second year.

Exploration of temperature drivers

We selected the CESM Last Millennium Ensemble (CESM-LME) and applied multiple linear regression (MLR)[49,50] for this attribution study due to its particular suitability for investigating climate variability over the Tibetan Plateau[26]. As demonstrated in previous studies[26], the CESM-LME outperforms other model ensembles (e.g., PMIP3) in simulating the temporal evolution and spatial patterns of TP temperature during the last millennium. This superior performance is attributed to its large ensemble size, which effectively captures internal variability, and its more comprehensive implementation of external forcings, particularly land-use/land-cover changes[51–53]. Therefore, the CESM-LME provides a robust and physically coherent framework for quantifying the contributions of external drivers to TP temperature changes. First, we extracted the historical temperature change series for the Tibetan Plateau regional temperature from both the full forcing and single forcing experiments. We then isolated the internal variability of potential drivers, such as the IPO and AMV, in the full forcing experiment. Both the single-forcing and internal variability series were standardized, and a 21-year filter was applied to remove dimensional differences. For a given time t, the regression equation can be expressed as:

$$R_{all}(t) = Residual(t) + \sum_{i=1}^{n}(R_{single}(t) \times \beta_i) \qquad (2)$$

The explanatory variance (EV) of the relative contributions was calculated as follows:

$$EV_i = \frac{|\beta_i|R^2}{\sum_{i=1}^{n}|\beta_i|} \times 100\% \qquad (3)$$

Among them, the IPO index is defined as the difference between SST anomalies in the central equatorial Pacific (170°E–90°W, 10°S–10°N) and the averages in the Northwest (140°E–145°W, 25°N–45°N) and Southwest Pacific (150°E–160°W, 50°S–15°S), capturing a characteristic "tripole" SST anomalies pattern on decadal timescales while efficiently tracking ENSO-related variations[54]. The IOD changes by calculating the difference in SST anomalies between the tropical western Indian Ocean (10°S–10°N, 50°E–70°E) and the equatorial southeastern Indian Ocean (10°S–0°, 90°E–110°E), with positive and negative phases identified as values beyond ±1 standard deviation[55]. The AMV index measures the SST difference between the North Atlantic (0°–65°N, 80°W–0°) and the global ocean mean, capturing long-term SST variations in the region[56]. The AO index, following Thompson and Wallace (1998), is derived as the first Empirical Orthogonal Function (EOF1) of 1000-hPa geopotential height anomalies poleward of 20°N, reflecting a dipole pattern of pressure anomalies between the Arctic and mid-latitudes[57].

To quantitatively detect and attribute the influence of anthropogenic forcing on Tibetan Plateau temperatures, we employed a fingerprint-based detection and attribution framework following Marvel[58–60]. This involved defining the expected forced response pattern (fingerprint) as the leading Empirical Orthogonal Function (EOF) of the CMIP6 multi-model (Supplementary Table 4) mean summer (JJAS) temperature under the SSP5-8.5 scenario (1850–2100). The temporal evolution of this fingerprint in the observations and reconstructions was quantified by calculating a projection time series, P(t) (Supplementary Fig. 8), which measures the spatial covariance between the gridded data D(t, θ, φ) and the fingerprint pattern F(θ, φ) according to the equation:

$$P(t) = \sum_{\theta,\varphi} D(t, \theta, \varphi)F(\theta, \varphi)w(\theta, \varphi) \qquad (4)$$

where $w(\theta,\varphi)$ is the grid region. If the searched fingerprint is found in the data, then $P(t)$ is trending upwards, and the signal (S) is the length trend in $P(t)$ is obtained by least squares regression[59]. The standard deviation of the pre-Industrial Revolution projection signal in our regional grid

reconstruction projection was taken as the noise (N), and then the signal was divided by the noise to obtain the signal-to-noise ratios (SNR). Under a one-sided Gaussian assumption, signal-to-noise ratios thresholds of 0.95, 1.64, and 2.57 correspond to detection at ~66% ("likely"), 90% ("very likely"), and 99% ("almost certain") confidence, respectively; exceeding a given threshold indicates detection at that level[60].

Relationship with streamflow

Monthly total streamflow records from 1970 to 2010 were obtained from the Kachura, Nuxia, and Daojieba hydrological stations, representing the Indus, Brahmaputra, and Salween basins, respectively (Supplementary Fig. 3b, d). To evaluate the relationship between summer mean (June–September) temperatures and streamflow, Pearson correlation analysis was conducted using both observed and reconstructed temperature data, covering the period from July of the previous year to February of the following year. Furthermore, probability density functions were utilized to evaluate and compare streamflow anomalies between the pre-industrial era and the modern period, providing insights into the hydrological impacts of long-term temperature changes. To further disentangle the causal pathways linking winter streamflow variability to subsequent summer temperature rise, we implemented a structural equation model (SEM). This multivariate framework enabled simultaneous testing of direct and indirect interactions among hydrological and thermal variables, accounting for temporal lags and latent feedback mechanisms[61]. The SEM integrated observed data from multiple sources, including total winter streamflow (Q) for the Indus, Brahmaputra, and Salween basins, gridded soil moisture (SM, 0–10 cm depth)[62] from January to September, Normalized Difference Vegetation Index (NDVI)[63], surface broadband albedo[64] and latent heat flux (LHF)[65] for June to September, and observed summer mean temperature (Tm) — with all gridded variables extracted for the core domain contained within 29-33°N and 92-95°E. Model validity was assessed using Chi-square, comparative fit index (CFI > 0.90), Tucker–Lewis Index (TLI > 0.92), Root Mean Square Error of Approximation (RMSEA < 0.05) and Probability level ($p > 0.05$)[66].

Data availability

Code availability

The code to perform these analyses is available from the corresponding authors upon request.

References

1. Khanal, S. et al. Variable 21st century climate change response for rivers in high mountain asia at seasonal to decadal time scales. *Water Resour. Res.* **57**, e2020WR029266 (2021).
2. Li, X. et al. Climate change threatens terrestrial water storage over the Tibetan Plateau. *Nat. Clim. Change* **12**, 801–807 (2022).
3. Wang, L. et al. The slowdown of increasing groundwater storage in response to climate warming in the Tibetan Plateau. *Npj Clim. Atmos. Sci.* **7**, 286 (2024).
4. Yao, T. et al. The imbalance of the Asian water tower. *Nat. Rev. Earth Environ.* **3**, 618–632 (2022).
5. Li, L., He, C., Li, J., Zhang, J. & Li, J. The supply and demand of water-related ecosystem services in the Asian water tower and its downstream area. *Sci. Total Environ.* **887**, 164205 (2023).
6. Dutta, P., Hinge, G., Marak, J. D. K. & Sarma, A. K. Future climate and its impact on streamflow: a case study of the Brahmaputra river basin. *Model. Earth Syst. Environ.* **7**, 2475–2490 (2021).
7. Shrestha, S., Bae, D.-H., Hok, P., Ghimire, S. & Pokhrel, Y. Future hydrology and hydrological extremes under climate change in Asian river basins. *Sci. Rep.* **11**, 17089 (2021).
8. Gupta, R. & Chembolu, V. Projecting socio-economic exposure due to future hydro-meteorological extremes in large transboundary river basin under global warming targets. *Water Resour. Manag.* https://doi.org/10.1007/s11269-024-04057-7 (2024).
9. Yang, K. et al. Recent climate changes over the Tibetan Plateau and their impacts on energy and water cycle: a review. *Glob. Planet. Change* **112**, 79–91 (2014).
10. Wu, X. et al. Attribution and risk projections of hydrological drought over water-scarce Central Asia. *Earths Future* **13**, e2024EF005243 (2025).
11. Chen, F. et al. Southeast Asian ecological dependency on Tibetan Plateau streamflow over the last millennium. *Nat. Geosci.* **16**, 1151–1158 (2023).
12. Wang, J., Yang, B. & Ljungqvist, F. C. A millennial summer temperature reconstruction for the eastern Tibetan Plateau from tree-ring width. *J. Clim.* **28**, 5289–5304 (2015).
13. Wang, J. et al. Tree-ring inferred annual mean temperature variations on the southeastern Tibetan Plateau during the last millennium and their relationships with the Atlantic Multidecadal Oscillation. *Clim. Dyn.* **43**, 627–640 (2014).
14. Liu, W. et al. Separating temperature from precipitation signals encoded in tree-ring widths over the past millennium on the northeastern Tibetan Plateau, China. *Quat. Sci. Rev.* **193**, 159–169 (2018).
15. Liu, Y. et al. Annual temperatures during the last 2485 years in the mid-eastern Tibetan Plateau inferred from tree rings. *Sci. China Ser. Earth Sci.* **52**, 348–359 (2009).
16. Bao, Y. & Brauning, A. Temperature variations on the Tibetan Plateau during the last millennium. *Adv. Clim. Change Res.* **3**, 31 (2007).
17. Xu, S. et al. A 903-year annual temperature reconstruction for the southeastern tibetan plateau from the tree ring widths of Juniperus saltuaria. *Sci. Rep.* **14**, 27623 (2024).
18. Büntgen, U. & Hellmann, L. The little ice age in scientific perspective: cold spells and caveats. *J. Interdisc. Hist.* **44**, 353–368 (2013).
19. Yue, W. et al. Late Ming Dynasty weak monsoon induced a harmonized megadrought across north-to-south China. *Commun. Earth Environ.* **5**, 439 (2024).
20. Huang, R. et al. A late summer temperature reconstruction based on tree-ring maximum latewood density since AD 1246 on the southeastern Tibetan Plateau. *Quat. Sci. Rev.* **355**, 109266 (2025).
21. Schmidt, G. A. et al. Climate forcing reconstructions for use in PMIP simulations of the Last Millennium (v1. 1). *Geosci. Model Dev.* **5**, 185–191 (2012).
22. Büntgen, U., Kirdyanov, A. V., Krusic, P. J., Shishov, V. V. & Esper, J. Arctic aerosols and the 'Divergence Problem' in dendroclimatology. *Dendrochronologia* **67**, 125837 (2021).
23. Büntgen, U. et al. Prominent role of volcanism in Common Era climate variability and human history. *Dendrochronologia* **64**, 125757 (2020).
24. Cook, E. R. et al. Asian monsoon failure and megadrought during the last millennium. *Science* **328**, 486–489 (2010).
25. Fallah, B. & Cubasch, U. A comparison of model simulations of Asian mega-droughts during the past millennium with proxy reconstructions. *Clim Past* **11**, 253–263 (2015).

26. Zuo, M., Zhou, T. & Man, W. Understanding surface temperature changes over the Tibetan Plateau in the last millennium from a modeling perspective. *Clim. Dyn.* **62**, 5483–5499 (2024).

27. Zhang, C. et al. Seasonal imprint of Holocene temperature reconstruction on the Tibetan Plateau. *Earth-Sci. Rev.* **226**, 103927 (2022).

28. Yin, H., Li, M.-Y. & Huang, L. Summer mean temperature reconstruction based on tree-ring density over the past 440 years on the eastern Tibetan Plateau. *Quat. Int.* **571**, 81–88 (2021).

29. Zhang, Y., Hao, Z., Xu, C.-Y. & Lai, X. Response of melt water and rainfall runoff to climate change and their roles in controlling streamflow changes of the two upstream basins over the Tibetan Plateau. *Hydrol. Res.* **51**, 272–289 (2020).

30. Cao, H. et al. Tree-ring insights into past and future streamflow variations in Beijing, Northern China. *Water Resour. Res.* **61**, e2024WR038084 (2025).

31. Zhang, Y., Gao, T., Kang, S., Shangguan, D. & Luo, X. Albedo reduction as an important driver for glacier melting in Tibetan Plateau and its surrounding areas. *Earth-Sci. Rev.* **220**, 103735 (2021).

32. Tang, S. et al. Regional and tele-connected impacts of the Tibetan Plateau surface darkening. *Nat. Commun.* **14**, 32 (2023).

33. Lin, Z. et al. Role of winter soil moisture in subsequent summer thermal anomalies on the Tibetan Plateau. *J. Clim.* **36**, 4739–4753 (2023).

34. Huang, J. et al. Global climate impacts of land-surface and atmospheric processes over the Tibetan Plateau. *Rev. Geophys.* **61**, e2022RG000771 (2023).

35. Yang, M., Wang, X., Pang, G., Wan, G. & Liu, Z. The Tibetan Plateau cryosphere: observations and model simulations for current status and recent changes. *Earth-Sci. Rev.* **190**, 353–369 (2019).

36. Fritts, H. *Tree Rings and Climate*. (Academic Press, 1976).

37. Cook, E. R. & Kairiukstis, L. A. *Methods of Dendrochronology: Applications in the Environmental Sciences* (Kluwer Academic Publishers, 1990).

38. Holmes, R. L. Computer-assisted quality control in tree-ring dating and measurement. *Tree-Ring Bull.* **43**, 69–78 (1983).

39. Schweingruber, F. H., Bartholin, T., Schaur, E. & Briffa, K. R. Radiodensitometric-dendroclimatological conifer chronologies from Lapland (Scandinavia) and the Alps (Switzerland). *Boreas* **17**, 559–566 (1988).

40. Homfeld, I. K., Büntgen, U., Reinig, F., Torbenson, M. C. & Esper, J. Application of RCS and signal-free RCS to tree-ring width and maximum latewood density data. *Dendrochronologia* **85**, 126205 (2024).

41. Wigley, T. M., Briffa, K. R. & Jones, P. D. On the average value of correlated time series, with applications in dendroclimatology and hydrometeorology. *J. Appl. Meteorol. Climatol.* **23**, 201–213 (1984).

42. Greenacre, M. et al. Principal component analysis. *Nat. Rev. Methods Prim.* **2**, 100 (2022).

43. Harris, I., Osborn, T. J., Jones, P. & Lister, D. Version 4 of the CRU TS monthly high-resolution gridded multivariate climate dataset. *Sci. Data* **7**, 109 (2020).

44. Sigl, M., Toohey, M., McConnell, J. R., Cole-Dai, J. & Severi, M. Volcanic stratospheric sulfur injections and aerosol optical depth during the Holocene (past 11 500 years) from a bipolar ice-core array. *Earth Syst. Sci. Data* **14**, 3167–3196 (2022).

45. Haurwitz, M. W. & Brier, G. W. A critique of the superposed epoch analysis method: its application to solar–weather relations. *Mon. Weather Rev.* **109**, 2074–2079 (1981).

46. Newhall, C. G. & Self, S. The volcanic explosivity index (VEI) an estimate of explosive magnitude for historical volcanism. *J. Geophys. Res. Oceans* **87**, 1231–1238 (1982).

47. Toohey, M. & Sigl, M. Volcanic stratospheric sulfur injections and aerosol optical depth from 500 BCE to 1900 CE. *Earth Syst. Sci. Data* **9**, 809–831 (2017).

48. Iles, C. E. & Hegerl, G. C. Systematic change in global patterns of streamflow following volcanic eruptions. *Nat. Geosci.* **8**, 838–842 (2015).

49. Otto-Bliesner, B. L. et al. Climate variability and change since 850 CE: an ensemble approach with the Community Earth System Model. *Bull. Am. Meteorol. Soc.* **97**, 735–754 (2016).

50. Zhou, J. & Tung, K.-K. Deducing multidecadal anthropogenic global warming trends using multiple regression analysis. *J. Atmos. Sci.* **70**, 3–8 (2013).

51. Chen, F. et al. Role of Pacific Ocean climate in regulating runoff in the source areas of water transfer projects on the Pacific Rim. *Npj Clim. Atmos. Sci.* **7**, 153 (2024).

52. Chen, F., et al. Coupled Pacific Rim megadroughts contributed to the fall of the Ming Dynasty's capital in 1644 CE. *Sci. Bull.* **69**, 3106–3114 (2024).

53. Wang, S., et al. Greening of Eurasia's center driven by low-latitude climate warming. *Forest Ecosyst.* **13**, 100330 (2025).

54. Henley, B. J. et al. A tripole index for the interdecadal pacific oscillation. *Clim. Dyn.* **45**, 3077–3090 (2015).

55. Saji, N. H., Goswami, B. N., Vinayachandran, P. N. & Yamagata, T. A dipole mode in the tropical Indian Ocean. *Nature* **401**, 360–363 (1999).

56. Deser, C. & Phillips, A. S. Defining the internal component of Atlantic multidecadal variability in a changing climate. *Geophys. Res. Lett.* **48**, e2021GL095023 (2021).

57. Thompson, D. W. J. & Wallace, J. M. The Arctic oscillation signature in the wintertime geopotential height and temperature fields. *Geophys. Res. Lett.* **25**, 1297–1300 (1998).

58. Hasselmann, K. Optimal fingerprints for the detection of time-dependent climate change. *J. Clim.* **6**, 1957–1971 (1993).

59. Santer, B. D. et al. Separating signal and noise in atmospheric temperature changes: the importance of timescale: TEMPERATURE SIGNAL-TO-NOISE RATIOS. *J. Geophys. Res. Atmos.* **116**, n/a–n/a (2011).

60. Marvel, K. et al. Twentieth-century hydroclimate changes consistent with human influence. *Nature* **569**, 59–65 (2019).

61. Wei, J. et al. Reduced growth of Qinghai spruce due to snow cover loss in high Asian elevations since the late 20th century. *J. Res.* **36**, 52 (2025).

62. McNally, A. et al. A land data assimilation system for sub-Saharan Africa food and water security applications. *Sci. Data* **4**, 170012 (2017).

63. Pinzon, J. E. & Tucker, C. J. A non-stationary 1981–2012 AVHRR NDVI3g time series. *Remote Sens.* **6**, 6929–6960 (2014).

64. Hersbach, H. et al. The ERA5 global reanalysis. *Q. J. R. Meteorol. Soc.* **146**, 1999–2049 (2020).

65. Gelaro, R. et al. The modern-era retrospective analysis for research and applications, version 2 (MERRA-2). *J. Clim.* **30**, 5419–5454 (2017).

66. Wang, X. et al. Disentangling the mechanisms behind winter snow impact on vegetation activity in northern ecosystems. *Glob. Change Biol.* **24**, 1651–1662 (2018).

Acknowledgements

Author contributions
F.C. and Y.C. conceived and designed the study, with input from all other authors. F.C. wrote the original draft. Y.C., M.H., X.Z., H.C., and S.W. performed the analyses and generated all the figures. All authors contributed to the discussions, editing the text reviews, and other improvements of this paper.

Competing interests

The authors declare no competing interests.

Additional information

Supplementary information The online version contains supplementary material available at https://doi.org/10.1038/s41612-025-01254-y.

Correspondence and requests for materials should be addressed to Feng Chen.

Reprints and permissions information is available at http://www.nature.com/reprints

Publisher's note Springer Nature remains neutral with regard to jurisdictional claims in published maps and institutional affiliations.